RSC Advances

PAPER

View Article Online
View Journal | View Issue

Cite this: *RSC Adv.*, 2023, **13**, 6619

A high-performance, oxidation resistance and flexible Zn@MXene/cellulose nanofibers electromagnetic shielding film†

Yunsheng Da,[ab] Qiqi Qu,[ab] Ling Kong,[b] Qiang Liu,[ab] Menghan Zhu,[ab] Yiming Du,[ab] Xingyou Tian,[a] Yanyan Liu*[a] and Hua Wang*[a]

Next-generation wearable electromagnetic interference (EMI) materials need to be provided with oxidation resistance, lightness, and flexibility. In this study, a high-performance EMI film with synergistic enhancement of Zn^{2+}@$Ti_3C_2T_x$ MXene/cellulose nanofibers (CNF) was found. The unique Zn@$Ti_3C_2T_x$ MXene/CNF heterogeneous interface facilitates the loss of interface polarization, making the total electromagnetic shielding effectiveness (EMI SE_T) and shielding effectiveness per unit thickness (SE/*d*) of the films reach 60.3 dB and 5025 dB mm^{-1}, respectively, in the X-band at the thickness of 12 μm ± 2 μm, significantly exceeding that of other MXene-based shielding materials. In addition, the coefficient of absorption gradually increases with the increasing CNF content. Moreover, under the synergistic effect of Zn^{2+}, the film shows excellent oxidation resistance (maintaining stable performance after 30 days), greatly exceeding the previous test cycle. Furthermore, the mechanical performance and flexibility of the film are greatly enhanced (tensile strength at 60 MPa, and maintaining stable performance after 100 times bending tests) due to the CNF and hot-pressing process. Therefore, with the enhancement of the EMI performance, high flexibility and oxidation resistance under high temperature and high humidity conditions, the as-prepared films have wide practical significance and broad application prospects in a series of complex applications, such as flexible wearable fields, ocean engineering fields and high-power device packaging fields.

Received 7th December 2022
Accepted 2nd February 2023

DOI: 10.1039/d2ra07791d

rsc.li/rsc-advances

1. Introduction

With the economic growth over the past several decades, it has become an increasingly common phenomenon to use wireless communication and intelligent electronic devices, conducing an invisible electromagnetic wave around us.[1–4] The electromagnetic radiation that is inevitably produced can bring harm because not only is the normal function and service life of electronic instruments badly affected, but the radiation is also a hazard to human health. To sort out the above issues, electromagnetic interference (EMI) shielding materials with good performance are urgently needed.[5–8] As a rule, reflected radiation is achieved only if typical EMI shielding materials directly interact with the electromagnetic fields and absorbing EM waves by internal electric and magnetic dipoles. Although traditional metal shielding materials possess excellent EMI shielding performance, they are limited in applications due to the inherent high density and corrosion susceptibility in harsh environments.[9–14] Recently, carbon nanotubes, graphene, MXene, and other related materials have been reported as potential alternatives for EMI shielding applications by virtue of their high aspect ratio, which can be used to fabricate highly flexible shielding films for flexible wearable fields.[15–20]

MXenes are two-dimensional (2D) nanosheets extracted by selectively etching the A-element from ternary transition metal carbides.[21–26] $M_{n+1}AX_n$ is the general formula, where M is the symbol of an early transition metal, A represents a group of XIII and XIV elements, and X is C and/or N. On the strength of the large specific surface area and high electrical conductivity, MXenes have exhibited lightweight and superior EMI shielding performance in previous research studies.[27] Through electrostatic adsorption, Song *et al.* generated honeycomb structural rGO-MXene/epoxy nanocomposites that showed an outstanding EMI shielding performance of 55 dB.[25] Ultra-light MXene aerogel/wood-derived porous carbon composites prepared by Liang *et al.* have been reported as achieving the optimal EMI SE value of up to 71.3 dB at a density as low as 0.197 g cm^{-3}.[13] Zeng *et al.* developed nanocellulose-MXene biomimetic aerogels, in which the EMI shielding effectiveness (SE) of the aerogels

[a]*Key Lab of Photovoltaic and Energy Conservation Materials, Institute of Solid State Physics, HFIPS, Chinese Academy of Sciences, 2221 Changjiang West Road, Shushan District, Hefei 230031, Anhui Province, China. E-mail: wanghua@issp.ac.cn; liuyanyan@rntek.cas.cn*

[b]*University of Science and Technology of China, Hefei 230026, People's Republic of China*

† Electronic supplementary information (ESI) available. See DOI: https://doi.org/10.1039/d2ra07791d

reaches 74.6 or 35.5 dB at a density of merely 8.0 or 1.5 mg cm^{-3}, respectively.[28] These lightweight three-dimensional network skeleton MXene-based composites are considered to have broad application prospects in the field of electronic material packaging, artificial intelligence and flexible equipment. However, in the practical application process, electromagnetic shielding materials usually face the high temperature, high humidity and high pressure. In addition, the materials would undergo various bending and deformations on the surface of the flexible equipment. These pose a challenge to the performance stability of the composites under a harsh external environment and in the process of use. In the MXene-based composites, the MXene usually tends to degrade gradually in humid air, water or at high temperature, and these three-dimensional skeleton structures are not beneficial to the performance maintenance after bending and deformation.[29,30] Furthermore, previous studies on electromagnetic shielding materials have rarely studied the oxidation resistance and flexibility of the materials at the same time. Therefore, it is valuable to comprehensively consider the electromagnetic shielding performance, oxidation resistance and flexibility of the MXene-based composite materials.

In order to solve the oxidation problem of MXene nanosheets under high temperature and humid environment, positive metal ions are usually introduced between the MXene sheets, and then metal ions bond with the oxygen-containing groups on the MXene nanosheets, thus inhibiting the oxidation of MXene nanosheets. Compared with Co and Ni, which are commonly used in the field of electromagnetic shielding, Zn has lower cost and high metal activity, making it easy to ionize in water to produce Zn^{2+}. In addition, in order to enhance the flexibility of the MXene-based composites, reinforcing materials with excellent mechanical properties are usually introduced. As a one-dimensional material, cellulose nanofibers are often used as a reinforcing component of composites due to its inherent excellent biocompatibility, simple preparation and high tensile strength.[31–33]

In this work, a high-performance EMI film material of multi-layer structure was found. Electrostatic adsorption, vacuum-assisted filtration, and hot-pressing are the three major methods used to prepare this Zn@$Ti_3C_2T_x$ MXene/CNF EMI film with mechanical tensile strength, flexibility, and great electrical conductivity. Evidence shows the fabricated multi-layer structure composite film possesses excellent electromagnetic shielding performance, improved mechanical properties and strong oxidation resistance. This article provides a new concept for flexible wearable fields, ocean engineering fields, and high power device packaging fields that is advanced with enhanced EMI shielding and oxidation resistance, and will broaden the application of the layered structure to some extent.

2. Experiment

2.1 Materials

Ti_3AlC_2 MAX was purchased from Yiyi Technology Co., Ltd (Jilin, China). Cellulose nanofibers (CNF, 0.8–2.0 μm length) were purchased from Tianjin WoodeIF Biotechnology Co., Ltd. Zinc power was purchased from Aladdin. Lithium fluoride (LiF, A.R.) was provided by Macklin. 37% hydrochloric acid (HCl, A.R.) was contributed by Aladdin. Absolute ethanol (EtOH, A.R.) was obtained from Fuyu Fine Chemistry Co., Ltd (Tianjin, China). Deionized water was used for all experiments. All of the reagents were used as received.

2.2 Preparation

Fig. 1 shows the preparation process of the flexible electromagnetic shielding film, including the etching and stripping of Ti_3AlC_2 MAX, self-assembly of Zn^{2+} and $Ti_3C_2T_x$ MXene nanosheets, and the preparation of the Zn@$Ti_3C_2T_x$ MXene/CNF film by vacuum-assisted filtration and hot-pressing.

2.2.1 Preparation of $Ti_3C_2T_x$ MXene. $Ti_3C_2T_x$ MXene was prepared on the basis of the LiF and HCl mixture. Firstly, 2 g of LiF was added to 30 mL 9 M HCl to prepare the aggregate solution. The LiF was gradually dissolved into the pellucid solution on stirring. Secondly, 3 g Ti_3AlC_2 MAX was deliberately added to water with vigorous stirring. Then, the compound was reacted at 25 °C for 36 hours. The resulting amalgam was centrifuged at 4000 rpm for 10 minutes. After that, the supernatant was poured off and the debris was re-dispersed by deionized water. Then, the suspension was centrifuged at 4000 rpm for 10 minutes repeatedly until the pH of the suspension liquid became about six. At last, the supernatant was resolutely stirred for 5 min, and centrifuged at 4000 rpm for 20 minutes. The supernatant was collected and named as $Ti_3C_2T_x$ MXene.

2.2.2 Preparation of Zn@$Ti_3C_2T_x$ MXene. Firstly, 200 mg of metallic zinc powder was added into 10 mL $Ti_3C_2T_x$ MXene solution, followed by ultrasonic treatment for 60 s. After that, the $Ti_3C_2T_x$ MXene and hydrolyzed zinc ions were stuck together by electrostatic self-assembly, and rapidly settled down at the bottom as showed in Fig. S4.† Thereby, 20 mL of HCl was added to wipe off the redundant zinc powder. Finally, the precipitate was obtained through vacuum filtration and freeze-dried for future preparation.

2.2.3 Preparation of the Zn@$Ti_3C_2T_x$ MXene/CNF film. The obtained Zn@ $Ti_3C_2T_x$ MXene was dissolved in 10 mL deionized water, and an appropriate amount of cellulose nanofiber was added for ultrasonic treatment for 10 minutes. Then, the compound was stirred for 6 hours at 40 °C. The resulting mixed solution was filtered through a vacuum filtration device to form a film. The Zn@ $Ti_3C_2T_x$ MXene/CNF composite film was obtained with an average thickness of 12 μm ± 2 μm by hot-pressing at 80 °C and 5 MPa for 2 hours. The samples with different CNF content were named as Z@MC-x, where x is the mass percent of CNF in the composite ($x = 10, 15, 20, 25, 30$). As a comparison, we prepared the Zn@MXene and MXene/CNF composite by the same method.

2.3 Characterization

Scanning electron microcopy (SEM) pictures of the Zn@MXene/CNF film were taken by field emission SEM (FESEM, Sirion200) with 10 kV accelerating voltage. High-resolution TEM (HRTEM) images of MXene were taken by transmission electron

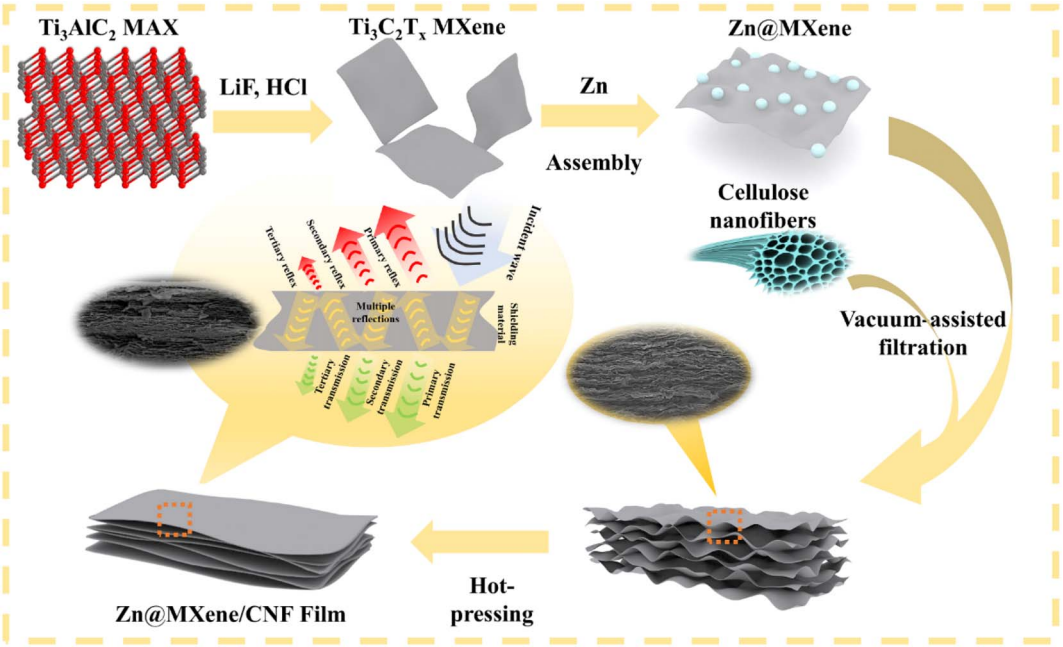

Fig. 1 The experimental process of preparing the Zn@MXene/CNF film.

microscope (TEM, JEM-2010, JEOL). The energy dispersive spectrometer (EDS) mapping pictures of the Zn@MXene/CNF film were obtained with a Schottky field emission scanning electron microscope (Gemini SEM 500) instrument. X-ray diffraction patterns were performed by X-ray diffractometer (XRD, Rigaku SMARTLAB 9 KW) of Ti_3AlC_2 MAX, $Ti_3C_2T_x$ MXene, Zn@$Ti_3C_2T_x$ MXene and Zn@MXene/CNF in the range of 5°–20°. X-ray photoelectron spectroscopy (XPS) measurements were performed by a Thermo Scientific Escalab Xi^+ X-ray photoelectron spectrometer. The EMI shielding performance was investigated through a vector network analyzer (Anritsu MS46322B) equipped with two waveguide-to-coaxial adaptors connected face to face. Electrical conductivity of the film samples was measured by a four-point probes electrical resistivity measurement system (RTS-9). The mechanical properties (*e.g.*, tensile strength) were evaluated by a tensile machine (CMT, SANS) according to ASTM D3039 at room temperature, and the splines used for characterization were cut to a size of 1 cm by 3 cm. The 100 bending tests for characterization of variations in the electromagnetic shielding properties of the composites were performed manually. The oxidation resistance of the composites is demonstrated by running a constant temperature and humidity chamber (WHTH-80-70-80) at 25 °C and 95% humidity for 30 days.

3. Results and discussion

3.1 Characterization of MXene and Zn@MXene/CNF films

Fig. 2a is the schematic diagram of the MXene layer spacing change. With the doping of Zn^{2+} and the introduction of CNF, the layer spacing between the MXene sheets gradually increases. Fig. 2b shows the XRD patterns of the MXene, Zn@MXene, and Z@MC-10 samples. It can be read that the (002) diffraction peak of MXene downshifts from 7.0° for pure MXene to 6.8° for Z@M and 6.5° for Z@MC-10, indicating a growth of interlayer spacing. In addition, manifested from the XPS spectra in Fig. 2c–e and S5,† C, the O, Ti and Zn elements coexist in the film. Triple doublets (Ti $2p_{3/2}$/Ti $2p_{1/2}$) that include Ti–C (461.1/455.0 eV), Ti(II) (462.7/456.1 eV) and Ti–O (464.4/458.3 eV) can be fitted by the high-resolution Ti 2p XPS spectrum of the Z@MC composite shown in Fig. 2c. As indicated in Fig. 2d, the C 1s core-level XPS spectrum can split into five peaks, namely C–Ti (281.8 eV), C–C (284.6 eV), C–Ti–O (282.3 eV), O–C–O (288.5 eV), and C–O (286.3 eV). Furthermore, from Fig. 2e of the core-level O 1s XPS spectrum, it reaches the peak at 530.2 eV with the Zn–O bond.[34] Zn^{2+} interplayed the oxygen-containing groups on MXene and CNF. This consequently spoiled the charge balance of the colloidal suspension. In that case, self-assembly occurs between the positively charge zinc ions and negatively charged MXene, as well as CNF. Fig. S1† shows the SEM image of $Ti_3C_2T_x$ MXene within the red region, which reveals that the pure $Ti_3C_2T_x$ MXene nanosheets illustrate a 2D lamellar structure with a flat and smooth surface. As determined from the HRTEM images in Fig. 2f, the interlayer spacing of the (002) crystal face of MXene is a 1.26 nm lattice fringe, which is in accordance with the result calculated by Bragg equation shown in Fig. S3.† In addition, as shown in Fig. S2† of the XRD patterns for Ti_3AlC_2 MAX and $Ti_3C_2T_x$ MXene, we can learn that the peaks of the (004), (101), (104), (105) crystal plane disappear, indicating the successful removal of Al and stripping of the MXene nanosheets. Fig. 2g, S6 and 2h, S7† show the SEM images of the composite films before hot-pressing and after hot-pressing. To further characterize the Z@MC composite, EDS element analysis was performed and is

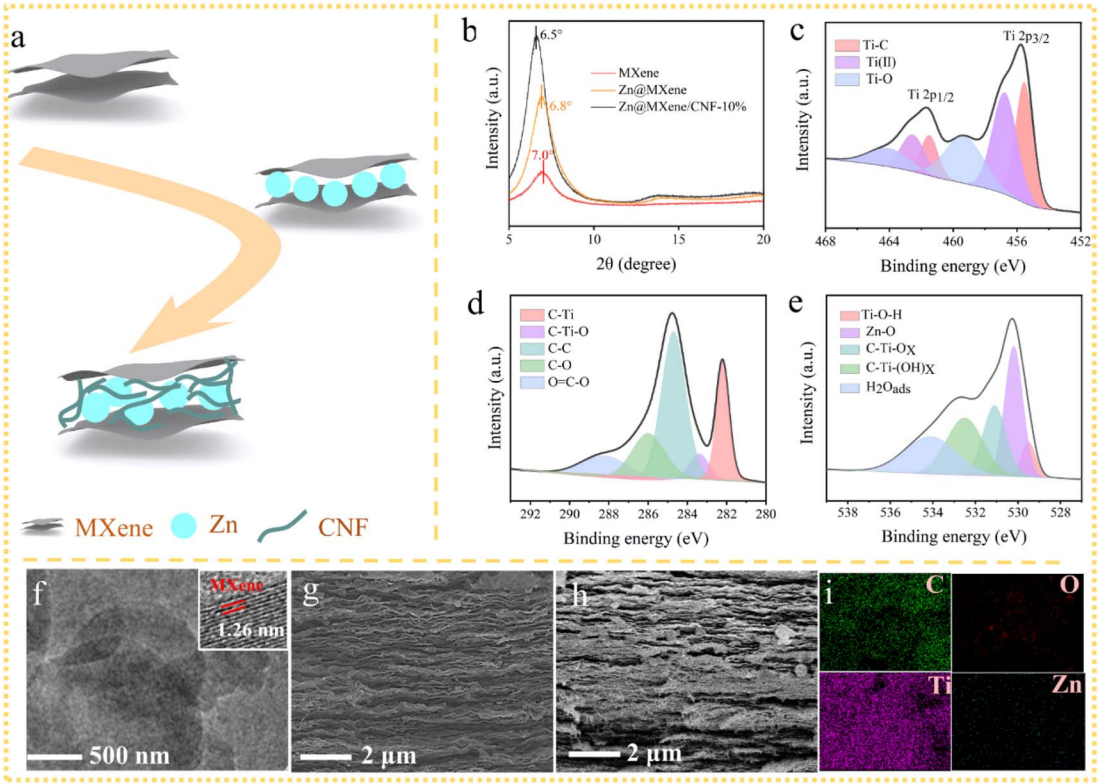

Fig. 2 (a) The schematic diagram of the $Ti_3C_2T_x$ MXene nanosheets with increasing lamellar spacing. (b) XRD patterns of the $Ti_3C_2T_x$ MXene, Zn@$Ti_3C_2T_x$ MXene, and Zn@$Ti_3C_2T_x$ MXene/CNF-10 samples. (c)–(e) XPS of the Zn@$Ti_3C_2T_x$ MXene/CNF-10 sample. (f) The HRTEM analysis of $Ti_3C_2T_x$ MXene. (g) SEM image for the cross-section of the film before hot-pressing. (h) SEM image for the cross-section of the film after hot-pressing. (i) Elemental mapping for C, O, Ti and Zn of the Zn@$Ti_3C_2T_x$ MXene/CNF composites.

shown in Fig. 2i. The corresponding mapping images show the uniform distribution of the C, Ti and O elements. Moreover, as suggested from the even distribution of the Zn element throughout the whole field of vision, the Zn element exists in the form of Zn^{2+} playing a role in crosslinking CNF and MXene nanosheets rather than aggregation state of Zn particles.

3.2 Electromagnetic shielding properties of the composite films

With the purpose of studying the effect of the microscopic layer spacing for the composite film on the performances, we explored the electrical conductivity and electromagnetic shielding performance of the Zn@MXene/CNF film with different CNF contents. As the XRD in Fig. S8† demonstrated, when the CNF content increased to 10% and 15%, the characteristic peak (002) of MXene located between 5–10° gradually moves to the left position. This phenomenon proves that the MXene lamella spacing was gradually enlarged as the CNF content is enhanced, in accordance with the result calculated by the Bragg equation shown in Fig. S9.† Interestingly, a slight improvement in the electromagnetic shielding performance and electrical conductivity for the composite films can be found from the results of Fig. 3a and S10.† This phenomenon can be explained by the formation of an insulating layer between the nanosheets from the inherent low electrical conductivity when introducing CNF. When the CNF content is relatively low, 10% for example, the insulating layer is extremely thin and bridges the MXene sheets. Carriers and electron holes efficiently migrate onto the MXene sheets in such a case. Thus, it indicates that an ultra-thin layer plays a role in promoting the electrical conductivity of the film. However, the interlayer spacing between the MXene expands more with further increase of CNF. In particular, when the CNF content is increased to higher than 20%, the insulating layer is thick enough to exceed the permeation threshold, inhibiting the migration of carriers and electron holes.

When testing the EMI shielding performance, the samples were a circle with a diameter of 3 mm in X-band (8–12 GHz). The total SE_T of the EMI shielding materials was determined by reflection efficiency (SE_R), absorption efficiency (SE_A) and multiple reflection efficiency (SE_M). The EMI SE_T can be expressed as:

$$SE_T = SE_R + SE_A + SE_M \quad (1)$$

However, the multiple reflections can be ignored ($SE_M \sim 0$) when the SE_T of the EMI shielding composite is more than 10 dB. The EMI SE_T can be expressed as:[35]

$$SE_T = SE_R + SE_A \quad (2)$$

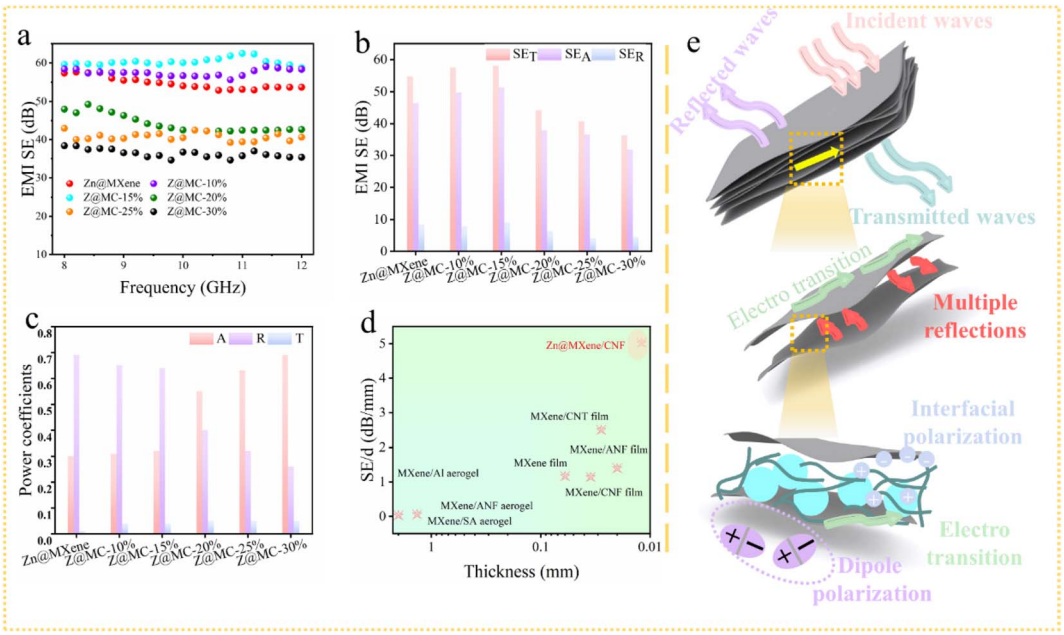

Fig. 3 (a) Electromagnetic shielding performance of Zn@MXene and Zn@$Ti_3C_2T_x$ MXene/CNF samples. (b) SE_T, SE_A and SE_R of Zn@MXene and Zn@$Ti_3C_2T_x$ MXene/CNF samples. (c) A, R, T of Zn@MXene and Zn@$Ti_3C_2T_x$ MXene/CNF samples. (d) Comparison of EMI SE_T per unit thickness among different MXene-based composite films in previous studies and this work. (e) Electromagnetic shielding mechanism.

The power coefficients of transmissivity (T), reflectivity (R), and absorptivity (A) can be calculated from the measured S-parameters, and their relationship is described as $R + T + A = 1$. Furthermore, the SE_R and SE_A can be expressed in the form of reflectance ($R = |S11|^2$) and transmittance ($T = |S21|^2$) as:[35]

$$SE_R = -10\log(1 - R) \quad (3)$$

$$SE_A = -10\log\left(\frac{T}{1 - R}\right) \quad (4)$$

The above-mentioned type of extremely thin insulating layer is also beneficial to promoting the electromagnetic shielding properties of the film. For example, the total EMI SE_T of the film can reach up to 60.3 dB with a 15 wt% increase of the CNF content. First, the maintained high conductivity level facilitates the reflective contribution of the electromagnetic shielding performance. Moreover, the electromagnetic shielding performance has an absorption efficiency at 51.3 dB, as shown in Fig. 3b. Owing to the existence of the insulating layer, more heterointerfaces are formed, leading to an enhanced interface polarization because of the large impedance mismatch. Correspondingly, the absorption contribution of the film to the incident waves gets reinforced. By and large, under the circumstance of the low CNF content, the insulating layer advances the electromagnetic shielding performance of the film. The electromagnetic shielding performance decreased to 38.4 dB when the CNF content reached 30 wt%. This drop suggests that the electromagnetic shielding properties of the composite films can be impaired by an excessive introduction of CNF. In addition, it can be found that the rather high ratio CNF of the film ineluctably reduced the conductivity and number of charge carriers. The EMI SE will be greatly ruined in this case. Simon formalism can be used to represent the EMI SET from formula (5), and the positive correlation between the EMI SET and conductivity is indicated from this Simon formalism:[34]

$$SE = SE_R + SE_A = 50 + 10\log\left(\frac{\sigma}{f}\right) + 1.7\delta\sqrt{\sigma f} \quad (5)$$

where σ is the electrical conductivity, and f is the frequency. Consistent with the aforementioned data analysis, the decrease of electrical conductivity of the composite can cause a performance drop of the electromagnetic shielding in the X-band.

Analysis towards the values of SE_R and SE_A in the X-band was made to further study the electromagnetic shielding mechanism. As observed from Fig. 3b, SE_R is much lower than SE_A, indicating SE_A (rather than SE_R) contributes to the electromagnetic shielding performance. When the CNF content is in the range of 15 wt%, the increase of the CNF content leads to an increased contribution made by SE_T and SE_A. Conversely, when the CNF content is over 15 wt%, the contribution of SE_T and SE_A changed to a falling trend. The above data analysis is consistent with the electromagnetic shielding performance and electrical performance. The reflectivity (R) and absorptivity (A) are quantitative characteristics of the power balance when an electromagnetic wave is incident on a shielding material. Fig. 3c shows the values of R, A, and T of the composite in a certain frequency. The value of R is much larger than that of A when the CNF content was lower than 15 wt%. This indicates the mechanism of the EMI shielding of reflection losses. On the other hand, once the CNF content was higher than 15 wt%, the value of A exceeds that of R, and the absorption loss mechanism of the EMI shielding is denoted. A small amount of cellulose can help

the conductivity of the composites maintain a high-level stability. First, the introduction of a small amount of CNF can form an ultra-thin insulating layer between the MXene nanosheets. This sandwich structure can be seen as a micro-capacitor, in which electrons can be rapidly transported.[36] The micro-capacitor plays a certain role in promoting the conductivity of the composites. In addition, the sandwich structure composed of MXene and CNF is conducive to the multiple reflections of the incident electromagnetic wave in the shielding body. More importantly, the heterogeneous interface between MXene and CNF also benefit the polarization loss of the electromagnetic waves. Therefore, in this case, the shielding mechanism of the composite is mainly reflection. When the content of cellulose increases to more than 15 wt%, the CNF insulation layer becomes thicker, which will inhibit the transmission of electrons and reduce the conductivity, resulting in a significant reduction in the reflection coefficient of the composites for electromagnetic waves. Therefore, in this case, the shielding mechanism of the composite is mainly absorption. In addition, as learned from the above Simon formula, a higher conductivity can effectively optimize the reflection loss of the composite material. There is a tremendous drop of the electrical conductivity that occurs when the cellulose content is higher than 20 wt%, damaging the conductive paths. Under this circumstance, a large number of heterogeneous interfaces stand between the cellulose nanofibers and Zn@MXene that exist in the composite material, and the polarization effect of the heterogeneous interfacial between the heterogeneous interfaces is profitable to the absorption loss of the composite material. Formulas (6) and (7) of the conductive monolithic materials can be used to determine the reflection losses and absorption losses, respectively, of the layered structure materials:[34]

$$SE_R = 168 - 10\log(f\mu_r\sigma_r) \quad (6)$$

$$SE_A = 131.4df\mu_r\sigma_r \quad (7)$$

where σ_r is the electrical conductivity of the shield relative to copper, μ_r is the magnetic permeability of the shield relative to free space ($\mu_0 = 4\pi \times 10^{-7}$ H m^{-1}), f is the frequency of the electromagnetic wave, and d is the shield thickness. It found that the reflection contributions increased with increasing conductivity. However, the absorption contributions are related to conduction, interfacial polarization, and magnetization.

To visually research the EMI shielding, various shielding mechanisms have been proposed, including the eddy current effect theory, electromagnetic field theory, and transmission line theory.[21–23] Among those studies, the transmission line theory is most widely recognized. According to the transmission line theory, electromagnetic waves that pass through the shielding materials will be affected by the three shielding mechanisms of reflection, absorption and multiple reflection. Fig. 3e exhibits the shielding process that occurs when the film interacts with the electromagnetic waves. When the electromagnetic waves were directed to the shielding material surface, the multi-layered structure and the hybridization of the zinc ions were synergistically enhanced. A portion of the electromagnetic waves is reflected because of the impedance mismatch between the shielding material. Electromagnetic waves that are not reflected enter the shielding material and are continuously attenuated. In the beginning, with the premium electrical conductivity, the films convert the penetrated electromagnetic waves into heat through ohmic loss. Ohmic loss connects to the energy attenuation that occurs *via* conduction, hopping and tunneling mechanisms, which advances the microwave absorption contribution. Moreover, with the enormous gap of conductivity between the Zn@MXene and CNF, considerable heterogeneous interfaces appeared as a result. Eventually, inside the composites, the electromagnetic waves undergo reflection multiple times, leading to energy dissipation. Based on the above outcome, the outstanding electrical conductivity of Z@MC and the multi-layered structure both support the improvement of the EMI shielding properties.

In order to compare the electromagnetic shielding performance of different systems, considering the low thickness of the film, the EMI SE of the composite films per unit thickness (SE/d) was calculated for comparison with other typical shielding materials, as shown in Fig. 3d and Table 1. The SE/d value in this work exceeds that of most reported MXene-based shielding materials. The information in Table 1 shows the effective comparison of the EMI shielding performance of these EMI shielding materials. For example, even at a high EMI SE of 60.3 dB, the SE/d value of the film is 5025 dB mm^{-1}, two orders of magnitude higher than most aerogel materials, and higher than that of most film materials. In addition, compared with the oxidation resistance characterization of MXene, this work has tested the oxidation resistance of the film for up to 30 days, greatly exceeding the previous test cycle. All of these observations indicate the superiority of the prepared film materials.

In addition, the effect of the macroscopic interlayer spacing on the performance of the composite film was explored. The effect of hot pressing on the material properties was explained in this work. As shown in the SEM images in Fig. S6 and S7,† after hot pressing, the interlayer spacing of the composite immensely diminished. As shown in Fig. 4a, the red and blue dotted lines indicate the tensile strength of the film before and after hot-pressing, respectively. It can be seen that the tensile strength of the film was significantly improved after hot-pressing. This is mainly due to the inherent excellent tensile strength and flexibility of CNF. During the hot-pressing process, the spacing between the multilayer structures in the film decreases, and CNF and the MXene sheets were combined more closely. These changes greatly promoted the tensile strength of the film. Moreover, with the increase of the CNF content, the tensile strength of the film increased more effectively by hot-pressing, which also shows the toughening effect of CNF as the adhesive among MXene sheets. From Fig. 4b, we defined the enhancement (%) as

$$\text{enhancement (\%)} = \frac{TS_{(\text{after hot-pressing})} - TS_{(\text{before hot-pressing})}}{TS_{(\text{before hot-pressing})}},$$

where TS is the tensile strength of the composite films. Interestingly, when the amount of CNF exceeds 20 wt%, the

Table 1 Comparison of theEMI SE_T per unit thickness among different MXene-based composite films in previous studies and this work

Composites	EMI SE_T (dB)	Thickness (mm)	SE/d (dB mm^{-1})	Oxidation-resistance
MXene/Al aerogel[37]	80	1.35	59.3	—
MXene/SA aerogel[38]	70.5	2	35.25	—
MXene/ANF aerogel[39]	65.5	2	32.75	2 hours
MXene film[40]	≈70	≈0.06	≈1167	—
MXene/ANF film[41]	28	0.02	1400	—
MXene/CNF film[42]	40	0.035	1142.9	—
MXene/CNT film[43]	70	0.028	2500	7 days
This work	**60.3**	**0.012**	**5025**	**30 days**

enhancement (%) of the film gradually decreases, which indicates that CNF has the best effect on improving the tensile strength of the film with 20 wt% load. This phenomenon is mainly related to the combination of CNF and MXene. In the process of preparation, the hydroxyl groups on the surface of CNF and the hydroxyl groups on the surface of MXene combine to form hydrogen bonds. CNF could enhance the interaction and promote the stress transfer, further leading to uniformly distributed stress in the composite film.[44] When the content of CNF is low, CNF can be uniformly distributed on the surface of MXene, which has a great positive impact on the enhancement of the tensile strength. However, when the content of CNF exceeds 20 wt%, there are also redundant self-tangled CNF, except for the CNF distributed on the surface of MXene nanosheets. This results in an uneven distribution of CNF, which has a certain inhibition effect on the enhancement of the tensile strength. Therefore, CNF has the best effect in improving the tensile strength of the film at 20 wt% loading.

Fig. 4c demonstrates that the EMI performance of the composite was greatly strengthened after hot pressing. The red and blue dotted lines in Fig. 4c represent the electromagnetic shielding performance of the pure MXene film before and after hot pressing, respectively. It can be observed that the electromagnetic shielding performance of the pure MXene film significantly drops from 24.7 to 18 dB after hot pressing. This is due to the Ti element on the surface of MXene oxidizing to form TiO_2, owing to the temperature and moisture. The intrinsically non-conductive TiO_2 hinders the electron migration between the MXene sheets, thereby reducing the conductivity and electromagnetic shielding performance of the film. The electromagnetic shielding performance is notably improved after hot pressing occurs in the thin film containing Zn^{2+}, as the Zn^{2+} ions work to bridge the MXene sheets and electrostatically absorbed onto the active sites on the surface of MXene, and then Ti is restricted from oxidation during hot pressing. The dramatic interfacial interactions after hot pressing explains the enhanced electromagnetic shielding performance of the film. It can be seen from Fig. 4c and d that introducing CNF into Zn@MX and hot pressing can effectively promote the electromagnetic shielding performance of the film. What is interesting is that promotion of the electromagnetic shielding performance was gradually enhanced after hot pressing with increasing CNF

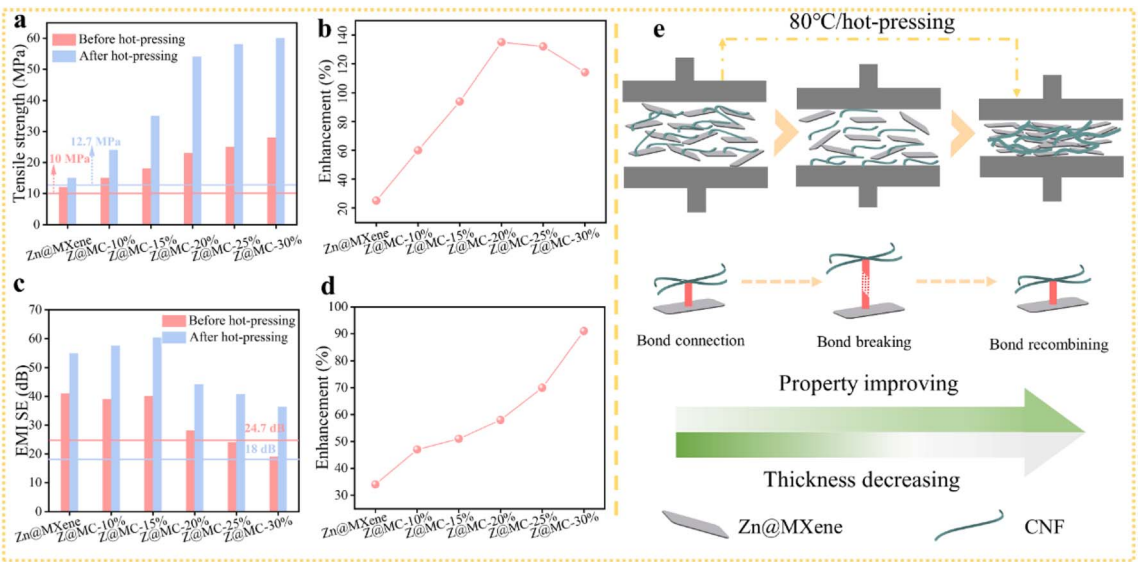

Fig. 4 (a) Variation of the tensile strength before and after hot-pressing. (b) Enhancement efficiency of the tensile strength by hot-pressing. (c) Variation of the electromagnetic shielding value before and after hot-pressing. (d) Enhancement efficiency of the electromagnetic shielding value by hot-pressing. (e) Schematic illustration of the interface recombination process between MXene and CNF during compression.

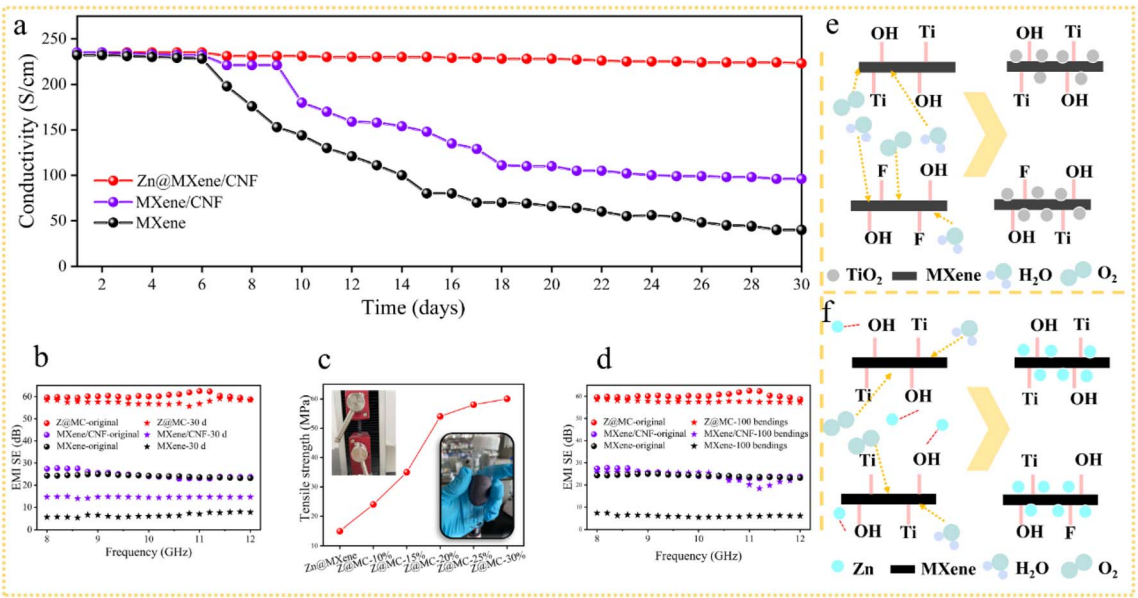

Fig. 5 (a) Variation in the conductivity of the Z@MC-15, MC-15, and pure MXene samples after 30 days. (b) Variation in the electromagnetic shielding performances of the Z@MC-15, MC-15 and pure MXene samples after 30 days. (c) Tensile strengths of the composites with different contents of CNF; the illustration shows the photograph of the tensile strength test of the composites and digital photograph of the composite film bending on the surface of the sample bottle. (d) Variation in the electromagnetic shielding performance of the Z@MC-15, MC-15 and pure MXene samples after 100 bending tests. (e and f) Oxidation mechanism and oxidation resistance mechanism of the MXene composite films and Z@MC composite films by oxygen and water.

content. There are two possible reasons for this result: the interfacial interaction between CNF and MXene becomes stronger, and the –OH groups on the surfaces of CNF and MXene form hydrogen bonds. This further minimizes the active sites on the MXene surface and prevents Ti from oxidation. In addition, with CNF as the binder, stacking between the faces of the MXene sheet decreases significantly during the interface reorganization.

To further explain the phenomenon of performance enhancement during hot-pressing, we propose a possible interface recombination mechanism as follows (Fig. 4e). It presumes that moisture has a hand in plasticizing to soften fiber and makes the composite material more easily compacted. At the start, mutual diffusion movement between Zn@MXene and CNF was gradually enhanced. Until the hydrogen bond breaks, the separation between the interfaces of Zn@MXene and CNF was completed. Accompanied with water evaporation and the slow cooling of the board after hot-pressing, Zn@MXene united CNF again to finish the intermolecular recombination process, and use of the cross-linking reagent was avoided in this way. The cross-linking effect of CNF explains the property improvement.

3.3 Oxidation resistance and flexibility of the film composites

To function normally and effectively, it is vital for electromagnetic shielding films to characterize the oxidation resistance under extreme conditions. That the composite material with Zn^{2+} hybridization possesses excellent oxidation resistance can be learned from Fig. 5a and b. This was proved by the absence of any tremendous reduction in the conductivity and electromagnetic shielding performance of Z@MC film when it was placed in a humid environment. Nevertheless, the pure MC film in humid surroundings had a sharp drop in conductivity and electromagnetic shielding performance. The high-density MXene films have good conductivity. As shown in Fig. 5e, the Ti on the surface of the MXene nanosheets will undergo oxidation reaction under the action of oxygen and water in the composite films without Zn^{2+}. The generated TiO_2 is not conductive at room temperature, thus reducing the conductivity and electromagnetic shielding performance of the films.[45] However, as shown in Fig. 5f, the combination of Zn^{2+} and oxygen-containing groups on the surface of the MXene nanosheets can effectively minimize the oxygen-containing terminal groups on the surface and edge of MXene in the composite films with Zn^{2+}. The reduction of oxygen-containing groups inhibits the oxidation reaction of Ti. More importantly, Zn^{2+} ions occupy the active sites on the surface of the MXene nanosheets, which hinders the nucleation of TiO_2 and further inhibits the oxidation reaction of Ti on the surface of the MXene nanosheets.[16,46,47] Therefore, compared with the result in Fig. 5e, the introduction of zinc ions plays a significant role in the oxidation resistance of the films.

To be qualified as an ideal substitute of EMI shielding and applied in next-generation smart protection equipment, the composite film materials require marvelous flexibility properties. Evaluation of the effect of applying composite materials for flexible materials in the future is essential. Along with introducing CNF, the tensile properties of the composite materials show a significant improvement. This is illustrated in Fig. 5c,

where the pure MXene film at 12 MPa is transferred to the Z@MC composites film at 60 MPa. By reorganizing the process of interfaces between MXene and CNF during hot-pressing along with CNF working as a connecting agent, the tensile strength of the composite material is evidently enhanced. Furthermore, the fatigue-proof property of the composite material in practical applications was simulated. Bending experiments performed 100 times were used to characterize the alternation in electromagnetic shielding properties of the composites. Fig. 5d shows that the shielding properties of the prepared composites were still maintained at quite a high level after the bending experiments. Compared to composites without CNF dropping to about 20 dB in bending experiments, the composites prepared in this work achieved stability on performance and excellent flexibility.

4. Conclusions

An oxidation resistant, ultra-thin and flexible Zn@MXene/cellulose nanofibers electromagnetic shielding film, composed of Zn^{2+}, MXene sheets and CNF, was manufactured by self-assembly, vacuum-assisted filtration and hot-pressing methods. The ingenious design of components and multilayer structure leads to great electromagnetic shielding performance, improved tensile strength and flexibility, and excellent oxidation resistance of the film. Owing to the unique Zn@$Ti_3C_2T_x$ MXene/CNF heterogeneous interfaces, Zn@MXene sheets and cellulose nanofibers, excellent EMI shielding performance was achieved. The composite films exhibited an X-band EMI SE of 60.3 dB at the thickness of 12 μm ± 2 μm. The SE/*d* value of the films reached 5025 dB mm^{-1}, significantly exceeding that of other MXene-based shielding materials. As a case in point, the Zn@$Ti_3C_2T_x$ MXene/CNF-15 composite features a total EMI shielding value of 60.3 dB and absorption efficiency of 51.3 dB, and also demonstrates an electric conductivity of 235.1 S cm^{-1}. Due to the multi-layer conductive structure of MXene and CNF and the synergistic enhancement of the hybrid zinc ions, the composite material prepared in this work exhibited excellent oxidation resistance for 30 days under 95% humidity and 25 °C, and improved tensile degree up to 60 MPa in the Zn@$Ti_3C_2T_x$ MXene/CNF-30 composite. In addition, the electromagnetic shielding performance of the materials is still stable after 100 bending tests, which indicates the great flexibility of this film. The Zn@MXene/CNF composite films have broad prospect in flexible wearable fields, ocean engineering fields and high-power device packaging fields.

Data availability

Data and materials are available upon request by contacting the author *via* e-mail at: dys0618@mail.ustc.edu.cn.

Author contributions

Yunsheng Da: conceptualization; methodology; investigation; formal analysis; data curation; visualization; roles/writing – original draft. Qiqi Qu: validation; visualization. Ling Kong: validation. Qiang Liu: methodology; supervision; software. Menghan Zhu: review & editing. Yiming Du: review; software. Xingyou Tian: review. Hua Wang: writing – review & editing; project administration; Yanyan Liu: validation; visualization.

Conflicts of interest

The authors declare that they have no known competing financial interests or personal relationships that could have appeared to influence the work reported in this paper.

Acknowledgements

This work is supported by the National Key R&D Program of China (No. 2017YFB0406200).

References

1 M. H. Al-Saleh and U. Sundararaj, Electromagnetic interference shielding mechanisms of CNT/polymer composites, *Carbon*, 2009, **47**(7), 1738–1746.
2 Y. Chen, *et al.*, Constructing a "pea-pod-like" alumina-graphene binary architecture for enhancing thermal conductivity of epoxy composite, *Chem. Eng. J.*, 2020, **381**, 122690.
3 Y. Cheng, *et al.*, A Flexible and Lightweight Biomass-Reinforced Microwave Absorber, *Nano-Micro Lett.*, 2020, **12**(1), 125.
4 C. Cui, *et al.*, Flexible and ultrathin electrospun regenerate cellulose nanofibers and d-$Ti_3C_2T_x$ (MXene) composite film for electromagnetic interference shielding, *J. Alloys Compd.*, 2019, **788**, 1246–1255.
5 Z. Cui, *et al.*, Lightweight MXene/Cellulose Nanofiber Composite Film for Electromagnetic Interference Shielding, *J. Electron. Mater.*, 2021, **50**(4), 2101–2110.
6 Y. Da, *et al.*, Novle layered boron nitride nanosheets/cellulose nanofibers/epoxy composite with high thermal conductivity, *High Perform. Polym.*, 2022, **34**(1), 87–94.
7 Y. Deng, *et al.*, Fast Gelation of $Ti_3C_2T_x$ MXene Initiated by Metal Ions, *Adv. Mater.*, 2019, **31**(43), 1902432.
8 M. Gouda, A. A. Hebeish and A. I. Aljaafari, New route for development of electromagnetic shielding based on cellulosic nanofibers, *J. Ind. Text.*, 2017, **46**(8), 1598–1615.
9 Q.-F. Guan, *et al.*, Sustainable Double-Network Structural Materials for Electromagnetic Shielding, *Nano Lett.*, 2021, **21**(6), 2532–2537.
10 L.-C. Jia, *et al.*, Electrically conductive and electromagnetic interference shielding of polyethylene composites with devisable carbon nanotube networks, *J. Mater. Chem. C*, 2015, **3**(36), 9369–9378.
11 X. Li, *et al.*, MXene/FeCo films with distinct and tunable electromagnetic wave absorption by morphology control and magnetic anisotropy, *Carbon*, 2021, **175**, 509–518.
12 Y. Lian, *et al.*, Solvent-Free Synthesis of Ultrafine Tungsten Carbide Nanoparticles-Decorated Carbon Nanosheets for Microwave Absorption, *Nano-Micro Lett.*, 2020, **12**(1), 153.

13 C. Liang, *et al.*, Ultra-light MXene aerogel/wood-derived porous carbon composites with wall-like "mortar/brick" structures for electromagnetic interference shielding, *Sci. Bull.*, 2020, **65**(8), 616–622.
14 C. Liang, *et al.*, Multifunctional Flexible Electromagnetic Interference Shielding Silver Nanowires/Cellulose Films with Excellent Thermal Management and Joule Heating Performances, *ACS Appl. Mater. Interfaces*, 2020, **12**(15), 18023–18031.
15 L. Liang, *et al.*, Multifunctional Magnetic $Ti_3C_2T_x$ MXene/Graphene Aerogel with Superior Electromagnetic Wave Absorption Performance, *ACS Nano*, 2021, **15**(4), 6622–6632.
16 Z. Lin, *et al.*, Highly Stable 3D $Ti_3C_2T_x$ MXene-Based Foam Architectures toward High-Performance Terahertz Radiation Shielding, *ACS Nano*, 2020, **14**(2), 2109–2117.
17 P. Liu, *et al.*, Synthesis of lightweight N-doped graphene foams with open reticular structure for high-efficiency electromagnetic wave absorption, *Chem. Eng. J.*, 2019, **368**, 285–298.
18 C. Ma, *et al.*, Wearable, ultrathin and transparent bacterial celluloses/MXene film with Janus structure and excellent mechanical property for electromagnetic interference shielding, *Chem. Eng. J.*, 2021, **403**, 126438.
19 B. Zhou, *et al.*, An asymmetric sandwich structural cellulose-based film with self-supported MXene and AgNW layers for flexible electromagnetic interference shielding and thermal management, *Nanoscale*, 2021, **13**(4), 2378–2388.
20 K. Chen, *et al.*, Multi-hierarchical flexible composites towards superior fire safety and electromagnetic interference shielding, *Nano Res.*, 2022, **15**(10), 9531–9543.
21 S. Ma, *et al.*, A high-performance, thermal and electrical conductive elastomer composite based on Ti3C2 MXene, *Composites, Part A*, 2021, **145**, 106292.
22 M. Parit, *et al.*, Polypyrrole and cellulose nanofiber based composite films with improved physical and electrical properties for electromagnetic shielding applications, *Carbohydr. Polym.*, 2020, **240**, 116304.
23 X. Pei, *et al.*, Porous network carbon nanotubes/chitosan 3D printed composites based on ball milling for electromagnetic shielding, *Composites, Part A*, 2021, **145**, 106363.
24 X. Shao, *et al.*, Tailoring of N-doped graphite coated cobalt nanoparticles via arc discharge enables high microwave absorption, *Carbon*, 2021, **177**, 171–180.
25 P. Song, *et al.*, Honeycomb structural rGO-MXene/epoxy nanocomposites for superior electromagnetic interference shielding performance, *Sustainable Mater. Technol.*, 2020, **24**, e00153.
26 B. Zhou, *et al.*, Flexible MXene/Silver Nanowire-Based Transparent Conductive Film with Electromagnetic Interference Shielding and Electro-Photo-Thermal Performance, *ACS Appl. Mater. Interfaces*, 2020, **12**(36), 40859–40869.
27 B. Zhou, *et al.*, Robust double-layered ANF/MXene-PEDOT:PSS Janus films with excellent multi-source driven heating and electromagnetic interference shielding properties, *Nano Res.*, 2022, **15**(10), 9520–9530.
28 Z. Zeng, *et al.*, Nanocellulose-MXene Biomimetic Aerogels with Orientation-Tunable Electromagnetic Interference Shielding Performance, *Adv. Sci.*, 2020, **7**(15), 2000979.
29 X. Jia, *et al.*, Construction of compressible Polymer/MXene composite foams for high-performance absorption-dominated electromagnetic shielding with ultra-low reflectivity, *Carbon*, 2021, **173**, 932–940.
30 Z. Lu, *et al.*, Micro-porous MXene/Aramid nanofibers hybrid aerogel with reversible compression and efficient EMI shielding performance, *Composites, Part B*, 2021, **217**, 108853.
31 H. Wang, *et al.*, Enhanced Rate Capability of Ion-Accessible $Ti_3C_2T_x$-NbN Hybrid Electrodes, *Adv. Energy Mater.*, 2020, **10**(35), 2001411.
32 X. Wang and P. Wu, Fluorinated Carbon Nanotube/Nanofibrillated Cellulose Composite Film with Enhanced Toughness, Superior Thermal Conductivity, and Electrical Insulation, *ACS Appl. Mater. Interfaces*, 2018, **10**(40), 34311–34321.
33 Y. Wang, *et al.*, General Fabrication of 3D Hierarchically Structured Bamboo-like Nitrogen-Doped Carbon Nanotube Arrays on 1D Nitrogen-Doped Carbon Skeletons for Highly Efficient Electromagnetic Wave Energy Attenuation, *ACS Appl. Mater. Interfaces*, 2020, **12**(36), 40692–40701.
34 S. Zhao, *et al.*, Highly Electrically Conductive Three-Dimensional $Ti_3C_2T_x$ MXene/Reduced Graphene Oxide Hybrid Aerogels with Excellent Electromagnetic Interference Shielding Performances, *ACS Nano*, 2018, **12**(11), 11193–11202.
35 X. Xu, *et al.*, Insights into the microstructures and reinforcement mechanism of nano-fibrillated cellulose/MXene based electromagnetic interference shielding film, *Cellulose*, 2021, **28**(6), 3311–3325.
36 B. D. Boruah, Roadmap of in-plane electrochemical capacitors and their advanced integrated systems, *Energy Storage Mater.*, 2019, **21**, 219–239.
37 X. Wu, *et al.*, Direct Ink Writing of Highly Conductive MXene Frames for Tunable Electromagnetic Interference Shielding and Electromagnetic Wave-Induced Thermochromism, *Nano-Micro Lett.*, 2021, **13**(1), 148.
38 X. Wu, *et al.*, Compressible, durable and conductive polydimethylsiloxane-coated MXene foams for high-performance electromagnetic interference shielding, *Chem. Eng. J.*, 2020, **381**, 122622.
39 Y. Du, *et al.*, Ultralight, highly compressible, thermally stable MXene/aramid nanofiber anisotropic aerogels for electromagnetic interference shielding, *J. Mater. Chem. A*, 2022, **10**(12), 6690–6700.
40 J. Liu, *et al.*, Hydrophobic, Flexible, and Lightweight MXene Foams for High-Performance Electromagnetic-Interference Shielding, *Adv. Mater.*, 2017, **29**(38), 1702367.
41 F. Xie, *et al.*, Ultrathin MXene/aramid nanofiber composite paper with excellent mechanical properties for efficient electromagnetic interference shielding, *Nanoscale*, 2019, **11**(48), 23382–23391.
42 B. Zhou, *et al.*, Flexible, Robust, and Multifunctional Electromagnetic Interference Shielding Film with

Alternating Cellulose Nanofiber and MXene Layers, *ACS Appl. Mater. Interfaces*, 2020, **12**(4), 4895–4905.

43 B. Li, *et al.*, Bicontinuous, High-Strength, and Multifunctional Chemical-Cross-Linked MXene/Superaligned Carbon Nanotube Film, *ACS Nano*, 2022, 19293–19304.

44 W.-T. Cao, *et al.*, Binary Strengthening and Toughening of MXene/Cellulose Nanofiber Composite Paper with Nacre-Inspired Structure and Superior Electromagnetic Interference Shielding Properties, *ACS Nano*, 2018, **12**(5), 4583–4593.

45 P. Zhang, *et al.*, 3D carbon-coated MXene architectures with high and ultrafast lithium/sodium-ion storage, *Energy Storage Mater.*, 2020, **29**, 163–171.

46 Q. Zhao, *et al.*, Flexible 3D Porous MXene Foam for High-Performance Lithium-Ion Batteries, *Small*, 2019, **15**(51), 1904293.

47 P. Zhang, *et al.*, In Situ Ice Template Approach to Fabricate 3D Flexible MXene Film-Based Electrode for High Performance Supercapacitors, *Adv. Funct. Mater.*, 2020, **30**(47), 2000922.